

Significance of the Mn-Oxidation State in Catalytic and Noncatalytic Promotional Effects of MnO_x Domains in Formic Acid Dehydrogenation on Pd/MnO_x Interfaces

Bartu Karakurt, Yusuf Kocak, Igor Lyubinetsky, and Emrah Ozensoy*

Cite This: *J. Phys. Chem. C* 2020, 124, 22529–22538

Read Online

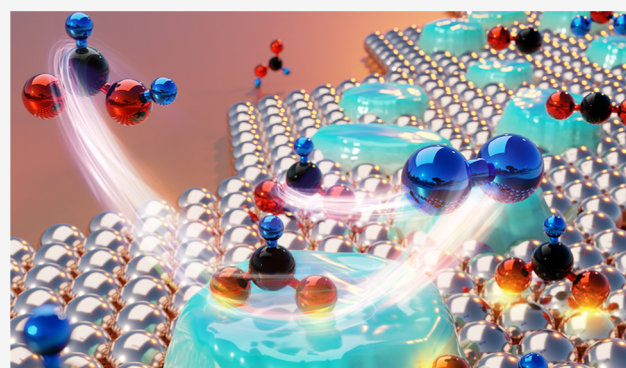
ACCESS |

Metrics & More

Article Recommendations

Supporting Information

ABSTRACT: The influence of MnO_x overlayers/nanoclusters deposited on the Pd(111) single-crystal model catalyst surface on the catalytic dehydrogenation of double-deuterated formic acid (FA, DCOOD) was studied under ultrahigh vacuum conditions *via* temperature-programmed desorption and X-ray photoelectron spectroscopy techniques. A significant boost in D₂ generation was observed in the catalytic FA dehydrogenation on MnO_x/Pd(111) as compared to that of a clean Pd(111) model catalyst, demonstrating the cooperative interaction between Pd(111) and MnO_x sites. Maximum FA conversion was observed at a submonolayer MnO_x surface coverage of 0.25 ML (monolayer) on Pd(111), whereas D₂ formation was found to be suppressed when the Pd(111) surface was entirely covered with relatively thick (15 ML) MnO_x overlayers. A direct correlation between increasing relative abundance of oxidized Mn surface states (*i.e.*, Mn²⁺, Mn³⁺, and Mn⁴⁺) and increasing catalytic FA dehydrogenation was observed. Different modes of promotion of FA dehydrogenation *via* MnO_x (*i.e.*, catalytic promotion versus noncatalytic/stoichiometric promotion) were discussed as a function of the differences in the model catalyst preparation and the extent of oxidation of the MnO_x overlayer.



1. INTRODUCTION

Formic acid (FA) is a promising hydrogen-based energy vector as it possesses a relatively high hydrogen content by mass (*i.e.*, 4.4 wt %) and exists in liquid form under ambient conditions, having low toxicity and low flammability.^{1,2} FA can be obtained from naturally abundant sources such as CO₂^{3,4} as well as renewable biomass feedstocks.⁵ These features render hydrogen production from FA a favorable option in various hydrogen energy applications.^{6,7} Catalytic decomposition of FA occurs *via* two competing pathways, namely dehydrogenation (HCOOH → H₂ + CO₂) and dehydration (HCOOH → H₂O + CO). As the FA dehydration pathway does not yield any H₂, catalytic selectivity toward H₂ is governed by the dominance of dehydrogenation over dehydration. In addition, CO generated as a result of dehydration can bind to the catalytically active noble metal sites (*e.g.*, Pd) in a strong and a rather irreversible manner at room temperature (RT), leading to site blocking and catalytic poisoning. Hence, the dehydration pathway significantly limits the catalytic selectivity and the catalyst life span.

FA decomposition on various late transition-metal surfaces such as Pd,^{8–12} Rh,^{13–15} Ru,^{16,17} Pt,^{18–20} Cu,^{21–23} Co,²⁴ Ag,²⁵ as well as Pd–Ag²⁶ and Pd–Au²⁷ bimetallic systems, has been extensively studied under ultrahigh vacuum (UHV) conditions. These studies showed that many high-coordination transition-

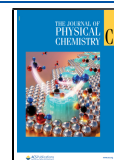
metal single-crystal surfaces were capable of carrying out FA dehydrogenation effectively.^{8,9,13,16,18,19} One of the key aspects associated with the catalytic action of these metal surfaces is their ability to stabilize the main FA decomposition intermediate, that is, formate.²⁸

Pd is known to be one of the most active catalytic metals that can efficiently generate ultrahigh purity hydrogen from biomass side products such as FA.^{29–32} The catalytic FA dehydrogenation performance of Pd-based heterogeneous catalytic systems is often improved *via* the introduction of additional bases into the reaction medium³³ or *via* the utilization of catalytic metal oxide promoters functionalized with basic groups in order to initiate the reaction and enhance selectivity toward H₂ formation.^{32,34,35} Former UHV studies on various single-crystal model catalysts revealed that the presence of Brønsted (*e.g.*, NH₃)⁸ and/or Lewis bases^{9,13,18} (*e.g.*, atomic O) can enhance the selectivity of group VIII transition-metal single-crystal surfaces toward FA dehydrogenation.

Received: July 29, 2020

Revised: September 16, 2020

Published: September 23, 2020



ation. In a former study,³⁶ we also showed that a high-surface-area mesoporous powder catalyst containing PdAg bimetallic nanoparticle active sites promoted with MnO_x nanodomains (dispersed on an amine-functionalized SiO₂ support) exhibited an extraordinarily high activity and selectivity in FA dehydrogenation at RT. Using *in situ* Fourier transform infrared (FTIR) spectroscopy, we demonstrated that³⁶ MnO_x promoter enhanced the catalytic FA decomposition over Pd active sites by (a) increasing FA adsorption on the catalyst surface through the formation of new FA adsorption sites, (b) facilitating FA deprotonation and formate production, (c) stabilization of the formate species on the catalyst surface, and (d) capturing/storing the catalytically generated CO(g) side product in the form of carbonates and preventing CO poisoning of the Pd active sites on which formate species are converted into the ultimately desired catalytic product, H₂. However, to this date, the relationship between the detailed electronic structure of the MnO_x domains and FA dehydrogenation performance has been mostly unknown.

Along these lines, in this study, the influence of MnO_x overlayers/nanoclusters deposited on a Pd(111) single-crystal model catalyst on catalytic FA dehydrogenation is investigated using surface-sensitive UHV experimental methods. In the current work, we show that the presence of a MnO_x/Pd(111) interface increases the hydrogen production as compared to a clean Pd(111) single-crystal model catalyst surface, where a correlation is established between the boosted catalytic performance and the extent of the oxidic character of the MnO_x surface states.

2. EXPERIMENTAL SECTION

2.1. Experimental Setup. Experiments were conducted in a custom-made UHV chamber with a base pressure of 1×10^{-10} Torr. The UHV chamber was equipped with the following modules: an X-ray photoemission spectroscopy (XPS; Riber Mg/Al dual anode X-ray source and a Riber EA 150 double pass cylindrical mirror electron energy analyzer) system, a custom-made low-energy electron diffraction optics, temperature-programmed desorption (TPD) instrument, temperature-programmed reaction spectroscopy (containing Ametek Dycor Dymaxion DM 200 quadrupole mass spectrometer and a Heatwave model 101303 PID-controlled linear sample heater) module, custom-made Mn thin-film evaporators, and an Ar⁺ ion gun (LK Technologies, NGI3000). Moreover, the UHV chamber also contained three separate gas dosing lines equipped with high-precision leak valves. The Pd(111) single-crystal sample (10 mm diameter \times 1 mm thickness disc, polished on both sides, purity > 99.999%, MaTeck GmbH) was affixed on Ta wires, which allowed cooling of the sample with liquid nitrogen to 90 K and heating it up to 1073 K *via* resistive heating. The temperature of the sample was measured by using a K-type thermocouple (thickness: 0.005 in., Omega Inc.) which was spot-welded on the upper side of the Pd(111) single crystal.

2.2. Cleaning of Pd(111) Single-Crystal Surface. Before each experiment, the Pd(111) sample surface was cleaned by using various methods depending on the extent of contaminations present on the surface of the Pd(111) sample. The first method consisted of multiple cleaning cycles, where Pd(111) was exposed to O₂(g) (Linde AG, purity \geq 99.999%) ($P_{O_2} = 1.0 \times 10^{-8}$ Torr, 5 min at 600 K) and subsequently annealed at 727 K for 5 min in vacuum. In the second method, after

exposing the Pd(111) sample to the conditions given above, the sample was flash-heated to 1000 K and then Ar⁺-sputtered (Ar(g), Linde AG, purity \geq 99.999%) with an ion gun (1.5 kV \times 15 mA) at RT, followed by annealing at 1000 K in UHV for 5 min. The third method included Ar⁺ sputtering at RT, followed by annealing at 1000 K in UHV for 5 min. The cleanliness of the Pd(111) surface was checked by performing blank TPD experiments, where the $m/z = 28$ desorption channel was monitored to verify the absence of strongly bound CO species on the surface before conducting the experiments.⁸

2.3. Utilization of Deuterated FA (DCOOD). DCOOD (FA-*d*₂, D > 98%, D₂O < 5%) was purchased from Cambridge Isotopes Laboratories Inc. (USA). The pristine DCOOD sample vial was initially opened inside a glovebox (*i.e.*, under a controlled atmosphere) and transferred into a UHV-compatible glass bulb equipped with a Swagelok VCR Nupro valve in order to prevent the exposure of DCOOD to atmospheric H₂O and CO₂. The UHV-compatible glass bulb was also covered with an Al foil to prevent possible photochemical reactions. Then, DCOOD(g) was introduced to the UHV chamber through a dedicated high-precision leak valve, using a fresh DCOOD dose before each TPD experiment as DCOOD is known to decompose upon its long-term interaction with stainless steel.⁹

2.4. Manganese Deposition and MnO_x Film Preparation. Before each experiment, metallic Mn(s) (MaTeck GmbH, Germany, Mn foil casted, purity: >99.9%) was thermally evaporated onto the clean Pd(111) single-crystal model catalyst surface at RT in UHV. The custom-made thermal evaporator had the dimensions of 1 mm \times 5 mm \times 1 mm and was operated with an input power of 1.5 V \times 12 A = 18 W *via* resistive heating. In the experiments where the MnO_x/Pd(111) surface was initially oxidized with O₂, Mn was first deposited on the clean Pd(111) substrate in UHV at RT. Then, this MnO_x/Pd(111) sample was flash-heated to 1000 K in UHV in order to mimic the morphology changes that might occur during the FA TPD experiments on MnO_x/Pd(111). Next, the MnO_x/Pd(111) system was exposed to 4.8×10^{-5} L of O₂ at 623 K (4×10^{-8} Torr \times 20 min) in front of the dedicated O₂ leak valve.

2.5. TPD and XPS Data Acquisition. TPD experiments were performed with a heating rate of 1 K/s. Multiplexing of each desorption channel during the TPD data acquisition was carried out using a dwell time of 30 ms. XPS measurements were performed by applying 250 W power to a Mg anode. The dwell time used for each energy step in the XPS measurement was 1 s, and each XPS spectrum was averaged over 15 scans.

3. RESULTS AND DISCUSSION

3.1. DCOOD Adsorption on Pd(111). The TPD profiles presented in Figure 1 were obtained by the adsorption of DCOOD, with an exposure of $\epsilon_{\text{DCOOD}} = 8 \times 10^{-3}$ L (1 L = 10^{-6} Torr s), on a clean Pd(111) surface at 123 K. Note that this particular FA exposure was chosen in order to be able to monitor all the relevant desorption features/products clearly (for instance, as shown in Figure S1, a relatively lower FA exposure of $\epsilon_{\text{DCOOD}} = 4 \times 10^{-3}$ L did not yield sufficiently strong desorption signals to effectively monitor all relevant reaction desorption channels), while minimizing the effects of water impurities in the FA feedstock, which can react with CO to replenish the poisoned Pd active sites.^{8,37} Figure 1 reveals the presence of $m/z = 4$ (D₂), $m/z = 30$ (DCO), and $m/z = 48$ (DCOOD) desorption signals, which is consistent with the

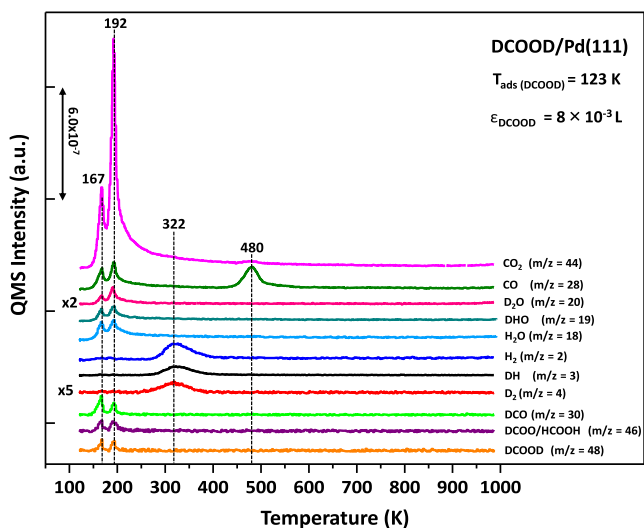


Figure 1. TPD profiles obtained upon a DCOOD exposure of 8×10^{-3} L at 123 K on clean Pd(111). Some of the desorption signals were multiplied with the given factors for better visualization.

adsorption of DCOOD on Pd(111).⁸ On the other hand, the occurrence of $m/z = 2$ (H_2) and $m/z = 3$ (DH) desorption signals indicates the presence of singly deuterated (DCOOH/HCOOD) and nondeuterated (HCOOH) FA species in the DCOOD feedstock and/or proton exchange events between DCOOD and the background H_2 and/or H_2O . It should be noted that the $m/z = 46$ desorption signal can be associated with both DCOO (*i.e.*, mass spectroscopic fragmentation of DCOOD) and molecular HCOOH species.

The TPD profiles shown in Figure 1 can be divided into four main desorption windows. The first desorption window is centered at *ca.* 167 K, and it is attributed to the desorption of catemeric/monomeric FA species formed on Pd(111).^{8,9} It should also be pointed out that the signals belonging to water species, that is, $m/z = 20$ (D_2O), $m/z = 19$ (DHO), and $m/z = 18$ (H_2O) signals, desorbing around 167 K are in line with the typical submonolayer water desorption from Pd(111).^{8,38} These species are assigned to the minor impurities in the FA

feedstock. Thus, the first desorption window is mostly due to the mass spectroscopic fragmentation of catemeric/monomeric FA units inside the quadrupole mass spectrometer rather than catalytic FA dehydrogenation/dehydration/decomposition reactions.⁸

In Figure 1, the second desorption window is centered at 192 K. The presence of a minor molecular FA desorption feature along with the appearance of intense CO_2 , D_2O , DHO, and H_2O signals (accompanied by D_2 , DH, and CO desorption signals observed at higher temperatures) suggests that FA is catalytically decomposed on Pd(111) at 192 K.^{8,26} Various experimental^{9,13,16,18} and theoretical^{39–41} studies on group VIII metal surfaces such as Pd(111) reported the formation of bidentate bridging formate species upon FA exposure. Consequently, the presence of an intense $m/z = 44$ (CO_2) signal at 192 K may suggest that the Pd(111) surface can decarboxylate the formate intermediate, facilitating FA dehydrogenation.⁸ However, simultaneous desorption of $m/z = 44$ (CO_2), $m/z = 20$ (D_2O), $m/z = 19$ (DHO), and $m/z = 18$ (H_2O) species at 192 K suggests that the Pd(111) single-crystal model catalyst is not 100% selective toward dehydrogenation. Note that the $m/z = 28$ (CO) signal at ≤ 192 K is attributed to the mass spectroscopic fragmentation of CO_2 as the line shapes of the corresponding $m/z = 44$ and $m/z = 28$ signals show significant resemblance, and CO desorption from the Pd(111) surface at submonolayer coverages occurs typically at much higher temperatures, such as 470–500 K, because of the strong chemisorption of CO on Pd(111).^{42–46}

The third desorption window in Figure 1 is centered around 320 K and it is due to the recombinative desorption of hydrogen species, that is, $m/z = 4$ (D_2), $m/z = 3$ (DH), and $m/z = 2$ (H_2), from the Pd(111) surface, which are generated as a result of dehydrogenation.^{8,9} In order to clarify the origin of $m/z = 2$ (H_2), the corresponding background H_2 desorption signal from a clean Pd(111) surface (*i.e.*, without any FA adsorption) was investigated in a control experiment (Figure S2). This control experiment revealed that H_2 adsorbed onto a clean Pd(111) surface from the background desorbed around 335 K, with the tail extending to higher temperatures.

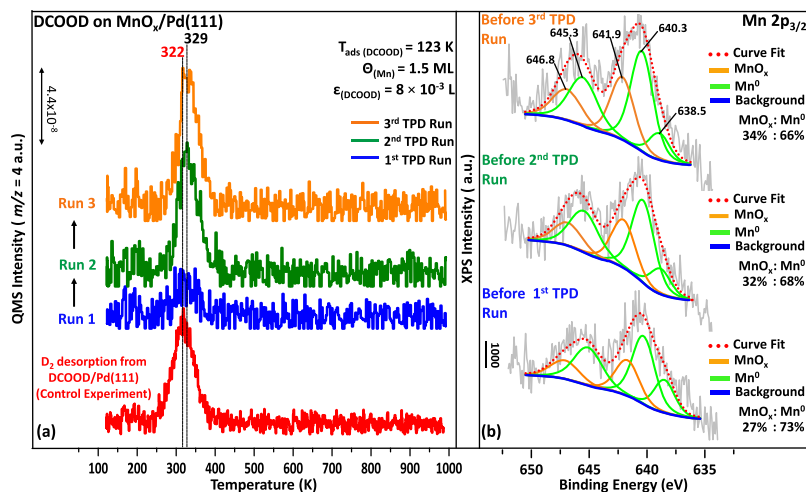


Figure 2. (a) TPD profiles showing the evolution of D_2 ($m/z = 4$) desorption signal upon three successive DCOOD adsorptions on $MnO_x(1.5 \text{ ML})/Pd(111)$ as compared to the control experiment performed on a clean Pd(111) surface under identical conditions. Before each TPD experiment, a fresh dose of DCOOD was adsorbed on $MnO_x(1.5 \text{ ML})/Pd(111)$ at 123 K ($\epsilon_{\text{DCOOD}} = 8 \times 10^{-3}$ L). (b) Corresponding Mn $2p_{3/2}$ XPS spectra of $MnO_x(1.5 \text{ ML})/Pd(111)$ obtained before the first, second, and third successive TPD runs (from bottom to top).

Corresponding differences in the desorption maxima and the lack of the high-temperature desorption tail in the $m/z = 2$ (H_2) desorption channel given in Figure 1 suggest that the $m/z = 2$ (H_2) desorption signal in Figure 1 is not due to background H_2 adsorption. Moreover, considering the different intensity scales in Figures 1 and S2, it is clear that the magnitude of H_2 desorption in the DCOOD/Pd(111) system is greater than that of the clean Pd(111) surface. Therefore, the $m/z = 2$ (H_2) desorption signal that is observed in Figure 1 was also classified as a dehydrogenation product.

Finally, the last temperature window in Figure 1 is positioned at *ca.* 480 K and reveals a relatively intense $m/z = 28$ desorption signal, whose desorption maximum is in accordance with the CO desorption observed upon the decomposition of FA on Pd(111).^{8,9} The absence of any $m/z = 44$ (CO_2) desorption signal at this temperature suggests that this species is not associated with CO_2 .⁸ Thus, it is apparent that while the first dehydration product (*i.e.*, H_2O , desorbing at $T \leq 192$ K) is bound relatively weakly to the Pd(111) surface, the second dehydration product (*i.e.*, CO, desorbing at 480 K) adsorbs extremely strongly on Pd(111) and blocks/poisons the surface.

3.2. D_2 Formation on $\text{MnO}_x/\text{Pd}(111)$. In order to investigate how the $\text{MnO}_x/\text{Pd}(111)$ surface differs from the clean Pd(111) surface in terms of D_2 generation capability and how D_2 generation evolves after consecutive reaction runs, 1.5 ML (monolayer) MnO_x was deposited on clean Pd(111) prior to FA exposure and investigated in a comparative fashion *via* TPD (Figure 2a) and XPS (Figure 2b). In these sets of experiments, three successive identical FA adsorptions were carried out on the MnO_x (1.5 ML)/Pd(111) surface. Before each FA exposure, XPS analysis was carried out, and after each FA exposure, TPD analysis was performed (see Section 2.4 and Figure S3 for further details regarding MnO_x deposition protocols and quantification of the MnO_x overlayer coverage on the Pd(111) surface). For $\theta_{\text{MnO}_x} < 1.5$ ML, the signal-to-noise ratio of the Mn $2p_{3/2}$ XP signal of the currently utilized photoelectron energy analyzer was low, rendering the accurate Mn oxidation state analysis *via* XPS rather difficult. Therefore, comparative XPS and TPD studies were performed at a MnO_x coverage of 1.5 ML, as shown in Figure 2. It should also be noted that the Pd $3p_{3/2}$ region (*ca.* 532 eV⁴⁷) of the XPS data overlaps with the O 1s species because of the manganese oxide domains (529.5–532 eV).⁴⁸ Thus, the deduction of conclusive information from the O 1s region of the XPS data regarding the detailed nature of the oxidized manganese overlayer species (such as the possible existence of $\text{Mn}(\text{OH})_x$ species) was not possible.

Figure 2b presents the Mn $2p_{3/2}$ XPS spectrum obtained after the 1.5 ML MnO_x deposition on Pd(111). It is well known that the Mn $2p_{3/2}$ XPS spectrum of metallic Mn has a single peak at *ca.* 638.8 eV.^{49–51} However, in the former studies regarding Mn overlayers grown on face-centered cubic (fcc) transition-metal surfaces (including Pd⁵²), the main Mn $2p_{3/2}$ XPS peak was observed at 640 eV and exhibited an intense satellite separated from the main feature by *ca.* +5 eV.^{53–55} Therefore, in Figure 2b, the peak located at 640.3 eV, along with the intense satellite feature at 645.3 eV, can be attributed to Mn^0 species. Moreover, earlier studies have also showed that the main Mn $2p_{3/2}$ XPS peak of Mn overlayers grown on Pd(100)⁵² and Ni(110)⁵³ exhibited an additional feature located below 640 eV, corresponding to the metallic Mn species that weakly interact with the fcc metal surface

underneath. Consequently, the lowest binding energy peak detected at 638.5 eV in Figure 2b is also attributed to Mn^0 species. The XPS spectra of manganese oxide overlayers grown on Pd(100) single-crystal surface showed a close resemblance to bulk manganese oxides,^{52,56} where Mn $2p_{3/2}$ peaks located at *ca.* 642 eV were mainly associated with the presence of Mn^{3+} and Mn^{4+} states in bulk manganese oxides.^{57–59} Furthermore, it was reported in earlier studies that the Mn^{2+} state had a distinct satellite feature around 647 eV.^{60–62} As a result of these findings, the presence of the broad peak located at 641.9 eV, along with an additional satellite feature occurring at *ca.* 647 eV, strongly suggests the presence of Mn^0 as well as oxidic Mn species (*i.e.*, Mn^{2+} , Mn^{3+} , and Mn^{4+}).⁶³

Therefore, the bottommost XPS spectrum in Figure 2b suggests that the deposited manganese overlayer was partially oxidized, where this partial oxidation can be tentatively attributed to the oxidation of Mn by the background water/hydroxide species generated due to the background pressure spike (*ca.* 1.5×10^{-9} Torr) that occurred during Mn thermal evaporation onto the Pd(111) substrate. The blue D_2 ($m/z = 4$) TPD profile given in Figure 2a, corresponding to the first of the three successive TPD runs, was obtained after FA adsorption on a freshly prepared MnO_x (1.5 ML)/Pd(111) surface. As can be seen from Figure 2a, the freshly prepared MnO_x (1.5 ML)/Pd(111) surface yielded a significantly smaller D_2 desorption signal as compared to that of the clean Pd(111) surface. Moreover, the presence of MnO_x domains also induced a shift in the D_2 desorption temperatures toward higher values, which can be attributed to the hindrance of hydrogen atom surface mobility.^{8,64} Importantly and contrary to the first observation, dosing a second identical exposure of DCOOD on the MnO_x (1.5 ML)/Pd(111) surface used in the first run (*i.e.*, spent surface) led to a significant increase in the D_2 formation in the second TPD run, and the D_2 desorption signal converged to a constant value in the third subsequent TPD run. It should be noted that the boost in D_2 formation in the second FA TPD run on the MnO_x (1.5 ML)/Pd(111) surface was also observed for other FA exposures and a variety of MnO_x coverages (*e.g.*, see Figures S4 and S5). In other words, this phenomenon was neither specific to a particular FA exposure nor a unique MnO_x coverage. Although this general behavior was observed for different MnO_x coverages, variation in the MnO_x coverage had an effect on the ultimate magnitude of the D_2 increase, as well as the number of runs it took for the D_2 signal to saturate (see Figure S4).

An additional control experiment also revealed that the observed phenomenon was not solely due to the thermally induced morphology changes in the MnO_x overlayer, such as the variations in the dispersion of the MnO_x overlayer on Pd(111) that might occur during the TPD temperature ramp in UHV. Along these lines, running the same reaction on a MnO_x (1.5 ML)/Pd(111) surface which was initially annealed in UHV at 1000 K for 1 min before FA exposure generated a smaller amount of D_2 with respect to the clean Pd(111) surface (Figure S6).

It should also be emphasized that the deposition of a relatively thick (*ca.* 15 ML) MnO_x overlayer, which presumably covered the entire Pd(111) surface, completely suppressed D_2 and DH formation, while substantially boosting the CO formation (Figure S7). This observation strongly suggested that MnO_x sites were not capable of enhancing D_2 formation on their own and the existence of MnO_x/Pd interfaces was essential for FA dehydrogenation.

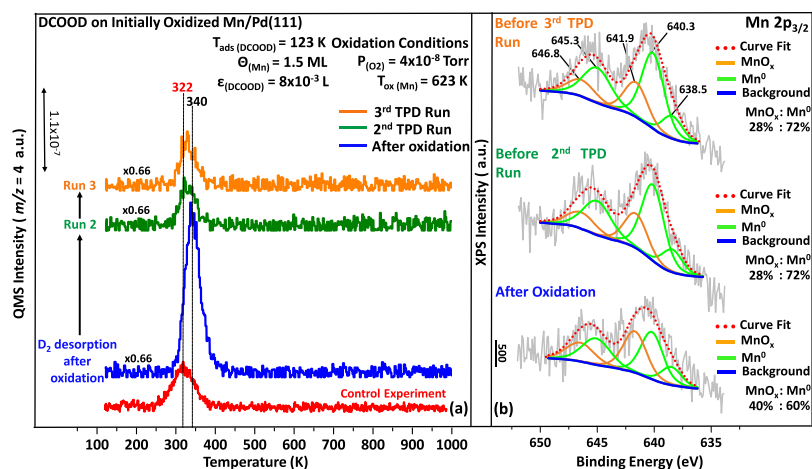


Figure 3. (a) TPD profiles showing the evolution of the $m/z = 4$ (D_2) desorption signal upon three successive DCOOD adsorptions on $\text{MnO}_x(1.5 \text{ ML})/\text{Pd}(111)$ which was initially oxidized with O_2 . Before each TPD experiment, a fresh dose of DCOOD was adsorbed on oxidized $\text{MnO}_x(1.5 \text{ ML})/\text{Pd}(111)$. (b) Corresponding Mn $2p_{3/2}$ XPS spectra obtained before each TPD experiment for $\text{MnO}_x(1.5 \text{ ML})/\text{Pd}(111)$ which was initially oxidized with O_2 . Some of the desorption signals were multiplied with the given factors for better visualization.

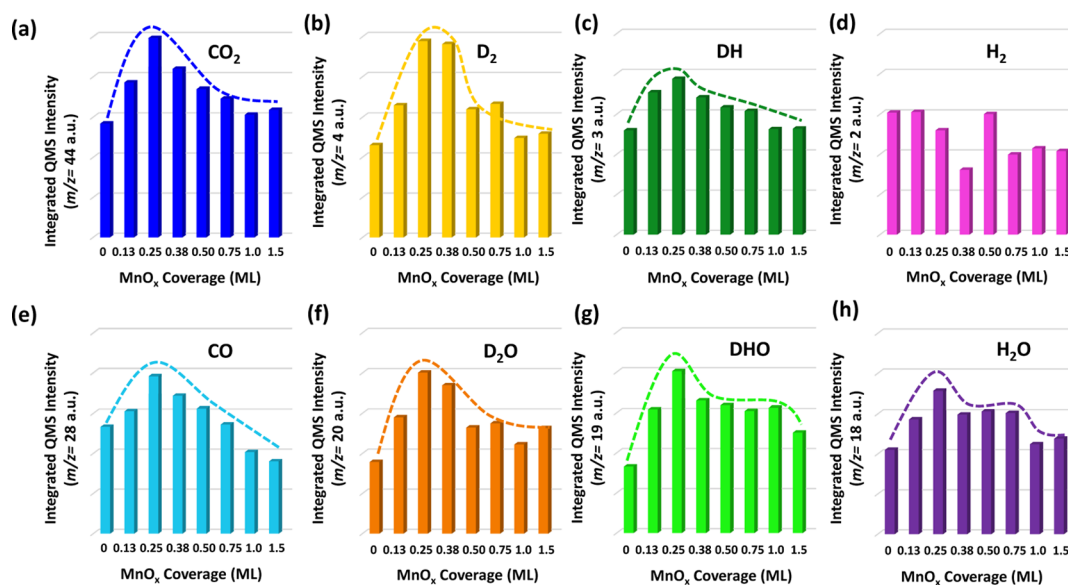


Figure 4. Integrated TPD desorption signals of various DCOOD ($T_{\text{DCOOD ads}} = 123$ K, $\epsilon_{\text{DCOOD}} = 8 \times 10^{-3}$ L) catalytic decomposition products on $\text{MnO}_x/\text{Pd}(111)$ model catalysts as a function of MnO_x overlayer coverage. Corresponding histograms for each MnO_x coverage were obtained by integrating the saturation TPD signal after the n th TPD run, yielding the maximum amount of desorption products for that particular MnO_x coverage.

The XPS spectrum in the middle of Figure 2b shows that before the second TPD run (*i.e.*, after the first FA adsorption and subsequent TPD run), the MnO_x overlayer was further oxidized. This is somewhat surprising as FA is not a well-known oxidizing agent. Furthermore, the oxidation of MnO_x was also accompanied by an increase in the overall Mn $2p_{3/2}$ XPS intensity, which could be attributed to the increased dispersion of the MnO_x overlayer on the Pd(111) substrate upon the first TPD temperature ramp to 1000 K (as in the case of a typical strong metal–support interaction). Similarly, the XPS spectrum obtained before the third TPD run, shown as the topmost spectrum in Figure 2b, indicated an additional but minor increase in the oxidic character of the MnO_x overlayer. These findings suggest that increasing the oxidic character of the MnO_x overlayer enhanced D_2 formation, implying that the oxidation state of MnO_x plays a crucial role in the D_2

production ability of the Pd/ MnO_x interface in FA dehydrogenation.

3.3. D_2 Formation on $\text{MnO}_x/\text{Pd}(111)$ Surface Oxidized with O_2 Prior to FA Exposure. As the findings discussed above indicated that the increase in the oxidic character of MnO_x promoted D_2 formation, an additional set of experiments was carried out on the $\text{MnO}_x(1.5 \text{ ML})/\text{Pd}(111)$ surface, where the freshly prepared $\text{MnO}_x(1.5 \text{ ML})/\text{Pd}(111)$ surface was oxidized *via* O_2 ($P_{\text{O}_2} = 4 \times 10^{-8}$ Torr, 623 K, 20 min) prior to FA dosing (Figure 3a,b). After the initial oxidation of the $\text{MnO}_x(1.5 \text{ ML})/\text{Pd}(111)$ surface with O_2 , three successive FA exposures were introduced on this model catalyst surface. Then, XPS/TPD analyses were performed before/after each FA dose. The bottommost Mn $2p_{3/2}$ XPS spectrum given in Figure 3b suggests that the $\text{MnO}_x(1.5 \text{ ML})/\text{Pd}(111)$ surface that was initially oxidized with O_2 prior to FA

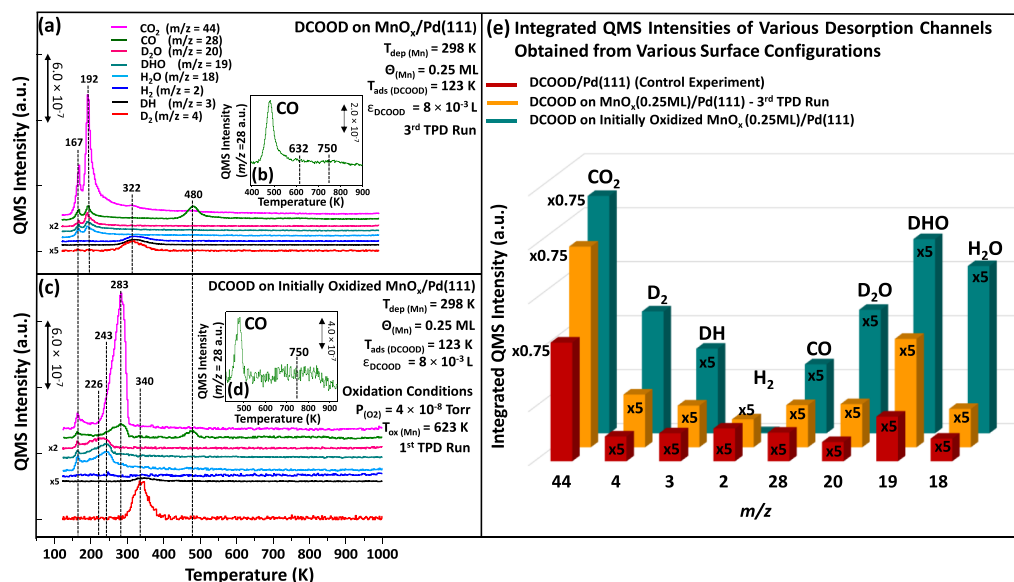


Figure 5. TPD data obtained for (a) third successive FA TPD run on MnO_x(0.25 ML)/Pd(111). (b) High-temperature portion (400–800 K) of the $m/z = 28$ (CO) desorption channel given in (a). (c) First FA TPD run over MnO_x(0.25 ML)/Pd(111) which was initially oxidized with O₂. (d) High-temperature portion (400–800 K) of the $m/z = 28$ (CO) desorption channel given in (c). (e) Integrated quadrupole mass spectrometry intensities of various desorption channels obtained from the indicated surfaces. Some of the data were multiplied with the given factors for better visualization.

adsorption had a MnO_x overlayer with the highest oxidic character among all other currently studied cases. Furthermore, the TPD profiles in Figure 3a clearly show that the oxidation of MnO_x with O₂ prior to FA adsorption caused an immediate boost in the D₂ formation. It should be noted that the initial oxidation with O₂ prior to FA adsorption also shifted the D₂ desorption maxima to higher temperatures (by *ca.* 20 K). This shift can be attributed to the hindrance of hydrogen atom mobility^{8,64} and stabilization of the formate intermediate by MnO_x oxidized with O₂ (see Figure 5c).

Unlike in Figure 2a, the reactivity boost due to initial oxidation with O₂ was observed only for the first TPD run in Figure 3a, and this boost diminished in the successive TPD runs. As a result of this observation, it can be argued that O₂ exposure can lead to the formation of more reactive but less stable MnO_x/Mn(OH)_x species compared to FA, where these more reactive species are depleted immediately after reacting with FA.

The XPS spectrum in the middle of Figure 3b indicates that, before the second TPD run (*i.e.*, after the oxidation step and the first TPD run), the oxidic character of MnO_x considerably decreased. On the other hand, the topmost XPS spectrum in Figure 3b suggests that, within our detection limits, the third reaction run caused a negligible change in the general oxidation state of the MnO_x overlayer as compared to that of the second run. As a result, it can be argued that the correlation between the increasing oxidic character of the MnO_x overlayer and enhanced FA dehydrogenation activity observed for MnO_x(1.5 ML)/Pd(111) in Figure 2 was also generally valid for the data given in Figure 3 for the MnO_x(1.5 ML)/Pd(111) surface which was initially oxidized with O₂.

3.4. Effects of MnO_x Coverage on Catalytic FA Decomposition. The influence of the MnO_x overlayer coverage on the catalytic FA decomposition ability of the MnO_x/Pd(111) model catalysts was also investigated. Hence, different MnO_x/Pd(111) model catalysts with varying MnO_x overlayer coverages were prepared, and the optimum MnO_x

overlayer coverage was determined. Figure 4 illustrates the integrated relative quantities of FA dehydrogenation and dehydration products (see Figure S8 for the associated TPD profiles and Table S1 for the integration temperature intervals used for the calculation of the histograms in Figure 4). One can see in Figure 4 that both the dehydration and dehydrogenation products followed a similar trend, having a maximum yield at the MnO_x coverage of 0.25 ML. It should be emphasized that a somewhat different trend was observed for the integrated H₂ production signals (which might be attributed to the influence of the background H₂ in the UHV chamber).

It is clear that the highest FA conversion was obtained for the MnO_x (0.25 ML)/Pd(111) surface. On this surface, the MnO_x overlayer had a submonolayer coverage and did not fully cover the Pd(111) substrate surface, allowing the existence of active Pd/MnO_x interfaces available for FA adsorption. Hence, it is clear that within $0 < \theta_{\text{MnO}_x} < 0.25$ ML, there exists a sufficiently large number of available/exposed Pd(111) active sites, and thus, catalytic performance increases monotonically with the increasing surface coverage of MnO_x domains which act as promoters. However, at coverages higher than $\theta_{\text{MnO}_x} > 0.25$ ML, because of the blocking of the Pd(111) active sites, the number of Pd(111) active sites decreases below the sufficient value and the catalytic performance starts to diminish.

3.5. Catalytic and Noncatalytic Promotional Effects of MnO_x on FA Decomposition over Pd(111). After having determined the optimum MnO_x overlayer coverage for DCOOD dehydrogenation on MnO_x/Pd(111) model catalysts as 0.25 ML, we investigated the detailed behavior of this particular MnO_x overlayer coverage in successive FA TPD runs in the absence (Figure 5a) and presence of initial oxidation with O₂ (Figure 5c).

The TPD data in Figure 5a,c correspond to two of the most active MnO_x(0.25 ML)/Pd(111) model catalysts obtained (i) after oxidation with FA (Figure 5a, third TPD run) and (ii) in

a single FA TPD run after initial oxidation with O₂ (Figure 5c, first TPD run). Comparison of these two different types of MnO_x(0.25 ML)/Pd(111) model catalysts (Figure 5a,c) with that of the clean Pd(111) surface (Figure 1) is given in Figure 5e. This comparison reveals that increasing the oxidic nature of the MnO_x overlayer either by successive FA TPD runs or *via* initial oxidation with O₂ leads to a simultaneous increase in both dehydrogenation and dehydration products and an increase in the overall total FA conversion (see Table S2 for the integration temperature intervals used for the calculation of the histograms given in Figure 5e).

Despite the fact that both of the MnO_x(0.25 ML)/Pd(111) model catalysts given in Figure 5a,c increase the overall FA conversion, surface chemistries of these differently prepared catalysts were quite dissimilar. First, the comparison of the CO₂ desorption signals for the FA TPD data of clean Pd(111) (Figure 1) and that of the third FA TPD run of MnO_x(0.25 ML)/Pd(111) (Figure 5a) points to the fact that when the MnO_x overlayer was oxidized *via* three successive FA TPD runs (Figure 5a), an additional high-temperature CO₂ desorption shoulder was observed at 322 K, which was absent in the case of clean Pd(111) (Figure 1). Moreover, the inset given in Figure 5b reveals the presence of an additional broad CO desorption feature that centers at *ca.* 750 K in Figure 5a, whereas these high-temperature CO features are absent for clean Pd(111) (Figure 1). In our former *in situ* FTIR studies,³⁶ we reported the formation of carbonates on the PdAg/MnO_x/SiO₂ and MnO_x/SiO₂ mesoporous powder catalysts upon CO adsorption. Therefore, the high-temperature CO₂ desorption features observed in Figure 5a and the high-temperature CO desorption features observed in Figure 5b can be attributed to the presence of adsorbed carbonate species on MnO_x domains, where the presence of CO and CO₂ desorption peaks around 750 K was also attributed to the presence of strongly bound carbonate species that are formed upon the adsorption of FA on K-promoted Rh(111) surface.⁶⁵ This observation suggests that this particular oxidic character of MnO_x can enhance FA adsorption and deprotonation,³⁶ where FA adsorbed on manganese oxide domains can eventually spillover onto the Pd(111) active sites, regenerating/unveiling the MnO_x adsorption sites for the next catalytic cycle. This particular performance-boosting action of the MnO_x overlayers can be considered to be a noncatalytic (*i.e.*, stoichiometric or sacrificial) effect, as this type of promotional effect is expected to gradually diminish as the MnO_x domains are continuously and irreversibly covered with strongly bound carbonate species. Accordingly, lack of significant differences in the desorption temperatures of the major desorption features of the clean Pd(111) single crystal (Figure 1) and that of the MnO_x(0.25 ML)/Pd(111) surface shown in Figure 5a also implies such a noncatalytic performance enhancement by MnO_x domains. In addition, the presence of high-temperature CO desorption features (Figure 5b) also suggests that MnO_x domains can act as sacrificial sites for CO adsorption³⁶ and hinder CO poisoning of the Pd(111) active sites.

On the other hand, as a manifestation of the differences in the oxidic nature of the MnO_x overlayers due to the variations in catalyst preparation protocols, catalytic promotional effects of the MnO_x domains can also be envisaged, particularly in the case of the MnO_x(0.25 ML)/Pd(111) surface which was initially oxidized with O₂ (Figure 5c). Similar to the case in which the MnO_x overlayer was oxidized *via* three successive FA TPD runs (Figure 5a), Figure 5d also reveals the presence

of high-temperature CO desorption signals which can be attributed to the presence of strongly adsorbed carbonate species.^{36,65} Unlike in Figure 5a, the major CO₂ desorption signal in Figure 5c was observed to shift to a significantly higher temperature of 283 K (along with a drastic growth in CO₂ desorption intensity) as compared to that of the clean Pd(111) surface, whereas the major CO₂ desorption signal appeared at 192 K in the latter case (Figure 1). This significant increase in the major CO₂ desorption temperature for the MnO_x(0.25 ML)/Pd(111) surface which was initially oxidized with O₂ (Figure 5b) implies that, when MnO_x is sufficiently oxidized, it can simultaneously improve FA adsorption/deprotonation and formate stability,^{8,9} positively contributing to the catalytic FA dehydrogenation.³⁹ Moreover, Figure 5c also reveals that oxidizing MnO_x with O₂ separates the desorption temperatures of water (243 K) and CO₂ (283 K) species, suggesting that oxidized MnO_x is also capable of decoupling the dehydrogenation and dehydration reactions that occur simultaneously on a clean Pd(111) surface (Figure 1) *via* improving formate stability. On the other hand, Figure 5c reveals that oxidizing MnO_x with O₂ also possibly triggers additional dehydration pathways (such as the condensation reactions of catemeric FA species, leading to the formation of water), once again showing that MnO_x does not selectively enhance catalytic FA dehydrogenation. As a result, the significant alterations that were observed in the FA decomposition chemistry after MnO_x oxidation with O₂ suggest that MnO_x can also catalytically contribute to FA decomposition when it is sufficiently oxidized. It should be noted that similar to the MnO_x overlayer that is oxidized *via* three successive FA TPD runs, the presence of high-temperature CO adsorption features implies that manganese oxide that was initially oxidized with oxygen can contribute to the enhanced catalytic FA conversion performance of MnO_x(0.25 ML)/Pd(111) by hindering CO poisoning of the Pd(111) active sites as well.

4. CONCLUSIONS

In the current work, we investigated catalytic FA decomposition on planar model catalyst surfaces composed of a MnO_x overlayer grown on a Pd(111) single crystal surface using various catalyst preparation protocols and compared the catalytic behavior of these systems to that of a clean Pd(111) benchmark catalyst. Increasing the oxidation state of the Mn³⁺ species in the MnO_x overlayer was found to boost both the dehydrogenation and dehydration pathways in a simultaneous manner. As a consequence of the differences in the surface chemistry and oxidation extent of the MnO_x overlayers on Pd(111) in different model catalyst preparation protocols, different promotional effects for MnO_x domains were proposed. In the case of the noncatalytic (*i.e.*, stoichiometric or sacrificial) promotional effect, MnO_x overlayers mainly serve as additional FA adsorption sites and facilitate FA adsorption/deprotonation, where FA that is adsorbed on the MnO_x domains can eventually spillover onto the Pd(111) active sites, regenerating/unveiling MnO_x adsorption sites for the next catalytic cycle. This particular promotional effect was observed for the moderately oxidic MnO_x overlayers on Pd(111). On the other hand, in the case of the catalytic promotional effect, highly oxidic MnO_x domains increased the formate stability and decoupled the dehydrogenation reaction from the dehydration reaction in terms of the corresponding product desorption temperatures. In all cases, MnO_x overlayers

also acted as CO capture domains, hindering CO poisoning of the Pd(111) active sites. The currently reported mechanistic results on MnO_x/Pd(111) model catalysts are in very good agreement with the former literature on high-surface-area powder catalysts containing Pd/MnO_x interfaces³⁶ and provide valuable molecular-level insights regarding the fundamental understanding of the promotional effects of MnO_x in the catalytic dehydrogenation of FA on Pd. Along these lines, current results can also be potentially applicable to the catalytic dehydrogenation of not only FA but also other organic acids or carboxylated oxygenates on different mesoporous high-surface-area transition-metal/metal oxide interfaces in order to design superior dehydrogenation catalysts to produce hydrogen from sustainable biomass feedstock.

■ ASSOCIATED CONTENT

Supporting Information

The Supporting Information is available free of charge at <https://pubs.acs.org/doi/10.1021/acs.jpcc.0c06942>.

TPD profiles obtained upon a relatively low DCOOD exposure of $\epsilon_{\text{DCOOD}} = 4 \times 10^{-3}$ L on clean Pd(111); $m/z = 2$ desorption channel from a blank (control) TPD experiment on a freshly cleaned Pd(111) surface in the absence of any intentionally introduced adsorbates; variation of the Mn 2p_{3/2}/Pd 3d integrated XPS intensity ratio of MnO_x/Pd(111) as a function of Mn deposition time; D₂ ($m/z = 4$) desorption channel in the TPD data upon three successive FA adsorption steps on MnO_x/Pd(111) with varying MnO_x surface coverages; variation of the D₂ ($m/z = 4$) desorption channel in the TPD data upon three successive DCOOD adsorption steps on MnO_x(0.25 ML)/Pd(111); change of the D₂ ($m/z = 4$) desorption signal in the TPD data upon two successive FA exposures of $\epsilon_{\text{DCOOD}} = 8 \times 10^{-3}$ L on a MnO_x(1.5 ML)/Pd(111) surface which was initially annealed in UHV at 1000 K for 1 min before the first TPD run; TPD profiles for DCOOD adsorption on MnO_x(15 ML)/Pd(111), where a very thick (multi-layer) MnO_x overlayer entirely covers/blocks the Pd(111) substrate; TPD profiles for DCOOD adsorption on MnO_x/Pd(111) as a function of MnO_x coverage; integration temperature intervals of the histograms given in Figure 4 of the main text; and integration temperature intervals of the histograms given in Figure 5e (PDF)

■ AUTHOR INFORMATION

Corresponding Author

Emrah Ozensoy – Department of Chemistry and UNAM-National Nanotechnology Center, Bilkent University, 06800 Ankara, Turkey; orcid.org/0000-0003-4352-3824; Email: ozensoy@fen.bilkent.edu.tr

Authors

Bartu Karakurt – Department of Chemistry, Bilkent University, 06800 Ankara, Turkey

Yusuf Kocak – Department of Chemistry, Bilkent University, 06800 Ankara, Turkey; orcid.org/0000-0003-4511-1321

Igor Lyubinetzky – Department of Chemistry, Bilkent University, 06800 Ankara, Turkey

Complete contact information is available at: <https://pubs.acs.org/doi/10.1021/acs.jpcc.0c06942>

Notes

The authors declare no competing financial interest.

■ ACKNOWLEDGMENTS

E.O. acknowledges the scientific collaboration with the TARLA project funded by the Ministry of Development of Turkey (project code: DPT2006K-120470). The authors also acknowledge Prof. Mehmet Erbudak (ETH Zurich) for his invaluable assistance with the UHV experimental setup. I.L. acknowledges The Scientific and Technological Research Council of Turkey (TUBITAK) and Horizon 2020 Marie Skłodowska-Curie CoCirculation2 Program for financial support (project code: 119C014). E.O. acknowledges the scientific collaboration with the TARLA project funded by the Republic of Turkey Presidential Directorate of Strategy and Budget (project code: 2006K12-827). The authors also acknowledge Mete Duman (UNAM-National Nanotechnology Center, Bilkent, Ankara, Turkey) for the design and production of the technical schematics.

■ REFERENCES

- (1) Eppinger, J.; Huang, K.-W. Formic Acid as a Hydrogen Energy Carrier. *ACS Energy Lett.* **2017**, *2*, 188–195.
- (2) Allsopp, M. W.; Vianello, G. Poly(Vinyl Chloride). *Ullmann's Encyclopedia of Industrial Chemistry*; Wiley-VCH Verlag GmbH, 2000.
- (3) Moret, S.; Dyson, P. J.; Laurenczy, G. Direct Synthesis of Formic Acid from Carbon Dioxide by Hydrogenation in Acidic Media. *Nat. Commun.* **2014**, *5*, 4017.
- (4) Ikemiya, N.; Natsui, K.; Nakata, K.; Einaga, Y. Long-Term Continuous Conversion of CO₂ to Formic Acid Using Boron-Doped Diamond Electrodes. *ACS Sustainable Chem. Eng.* **2018**, *6*, 8108–8112.
- (5) Valentini, F.; Kozell, V.; Petrucci, C.; Marrocchi, A.; Gu, Y.; Gelman, D.; Vaccaro, L. Formic Acid, a Biomass-Derived Source of Energy and Hydrogen for Biomass Upgrading. *Energy Environ. Sci.* **2019**, *12*, 2646–2664.
- (6) Brieger, G.; Nestrick, T. J. Catalytic Transfer Hydrogenation. *Chem. Rev.* **1974**, *74*, 567–580.
- (7) Zhang, D.; Ye, F.; Xue, T.; Guan, Y.; Wang, Y. M. Transfer Hydrogenation of Phenol on Supported Pd Catalysts Using Formic Acid as an Alternative Hydrogen Source. *Catal. Today* **2014**, *234*, 133–138.
- (8) Karakurt, B.; Kocak, Y.; Ozensoy, E. Enhancement of Formic Acid Dehydrogenation Selectivity of Pd(111) Single Crystal Model Catalyst Surface via Brønsted Bases. *J. Phys. Chem. C* **2019**, *123*, 28777–28788.
- (9) Davis, J. L.; Barteau, M. A. Reactions of carboxylic acids on the Pd(111)-(2 × 2)O surface: multiple roles of surface oxygen atoms. *Surf. Sci.* **1991**, *256*, 50–66.
- (10) Kovács, I.; Kiss, J.; Solymosi, F. On the Role of Adsorbed Formate in the Oxidation of C1 Species on Clean and Modified Pd(100) Surfaces. *Vacuum* **2017**, *138*, 152–156.
- (11) Solymosi, F.; Kovács, I. Adsorption and reaction of HCOOH on K-promoted Pd(100) surfaces. *Surf. Sci.* **1991**, *259*, 95–108.
- (12) Jorgensen, S. W.; Madix, R. J. Active oxygen on Group VIII metals: activation of formic acid and formaldehyde on Pd(100). *J. Am. Chem. Soc.* **1988**, *110*, 397–400.
- (13) Houtman, C.; Barteau, M. A. Reactions of formic acid and formaldehyde on Rh(111) and Rh(111)-(2 × 2)O surfaces. *Surf. Sci.* **1991**, *248*, 57–76.
- (14) Solymosi, F.; Kiss, J.; Kovács, I. Adsorption and Decomposition of Formic Acid on Potassium-Promoted Rhodium(111) Surfaces. *J. Phys. Chem.* **1988**, *92*, 796–803.
- (15) Solymosi, F.; Kiss, J.; Kovács, I. Adsorption of HCOOH on Rh(111) and its reaction with preadsorbed oxygen. *Surf. Sci.* **1987**, *192*, 47–65.

- (16) Avery, N. R.; Toby, B. H.; Anton, A. B.; Weinberg, W. H. Decomposition of formic acid on Ru(001): An eels search for a formic anhydride intermediate. *Surf. Sci.* **1982**, *122*, L574–L578.
- (17) Sun, Y. K.; Weinberg, W. H. Catalytic decomposition of formic acid on Ru(001): Transient measurements. *J. Chem. Phys.* **1991**, *94*, 4587–4599.
- (18) Avery, N. R. Adsorption of formic acid on clean and oxygen covered Pt(111). *Appl. Surf. Sci.* **1982**, *11–12*, 774–783.
- (19) Columbia, M. R.; Thiel, P. A. The reaction of formic acid with clean and water-covered Pt(111). *Surf. Sci.* **1990**, *235*, 53–59.
- (20) Silbaugh, T. L.; Karp, E. M.; Campbell, C. T. Energetics of Formic Acid Conversion to Adsorbed Formates on Pt(111) by Transient Calorimetry. *J. Am. Chem. Soc.* **2014**, *136*, 3964–3971.
- (21) Bowker, M.; Rowbotham, E.; Leible, F. M.; Haq, S. The Adsorption and Decomposition of Formic Acid on Cu {110}. *Surf. Sci.* **1996**, *349*, 97–110.
- (22) Yao, Y.; Zaera, F. Adsorption and thermal chemistry of formic acid on clean and oxygen-predosed Cu(110) single-crystal surfaces revisited. *Surf. Sci.* **2016**, *646*, 37–44.
- (23) Ying, D.; Robert, J. M. Thermal desorption study of formic acid decomposition on a clean Cu(110) surface. *J. Catal.* **1980**, *61*, 48–56.
- (24) Sims, J. J.; Ould Hamou, C. A.; Réocreux, R.; Michel, C.; Giorgi, J. B. Adsorption and Decomposition of Formic Acid on Cobalt(0001). *J. Phys. Chem. C* **2018**, *122*, 20279–20288.
- (25) Barteau, M. A.; Bowker, M.; Madix, R. J. Acid-base reactions on solid surfaces: The reactions of HCOOH, H₂CO, and HCOOCH₃ with oxygen on Ag(110). *Surf. Sci.* **1980**, *94*, 303–322.
- (26) Karatok, M.; Duanmu, K.; O'Connor, C. R.; Boscoboinik, J. A.; Sautet, P.; Madix, R. J.; Friend, C. Tuning Reactivity Layer-by-Layer: Formic Acid Activation on Ag/Pd(111). *Chem. Sci.* **2020**, *11*, 6492–6499.
- (27) Yu, W.-Y.; Mullen, G. M.; Flaherty, D. W.; Mullins, C. B. Selective Hydrogen Production from Formic Acid Decomposition on Pd–Au Bimetallic Surfaces. *J. Am. Chem. Soc.* **2014**, *136*, 11070–11078.
- (28) Shustorovich, E.; Bell, A. T. An Analysis of Formic Acid Decomposition on Metal Surfaces by the Bond-Order-Conservation-Morse-Potential Approach. *Surf. Sci.* **1989**, *222*, 371–382.
- (29) Choi, B.-S.; Song, J.; Song, M.; Goo, B. S.; Lee, Y. W.; Kim, Y.; Yang, H.; Han, S. W. Core–Shell Engineering of Pd–Ag Bimetallic Catalysts for Efficient Hydrogen Production from Formic Acid Decomposition. *ACS Catal.* **2018**, *9*, 819–826.
- (30) Bi, Q.-Y.; Lin, J.-D.; Liu, Y.-M.; He, H.-Y.; Huang, F.-Q.; Cao, Y. Dehydrogenation of Formic Acid at Room Temperature: Boosting Palladium Nanoparticle Efficiency by Coupling with Pyridinic-Nitrogen-Doped Carbon. *Angew. Chem., Int. Ed.* **2016**, *55*, 11849–11853.
- (31) Jiang, Y.; Fan, X.; Chen, M.; Xiao, X.; Zhang, Y.; Wang, C.; Chen, L. AuPd Nanoparticles Anchored on Nitrogen-Decorated Carbon Nanosheets with Highly Efficient and Selective Catalysis for the Dehydrogenation of Formic Acid. *J. Phys. Chem. C* **2018**, *122*, 4792–4801.
- (32) Bulut, A.; Yurderi, M.; Karatas, Y.; Zahmakiran, M.; Kivrak, H.; Gulcan, M.; Kaya, M. Pd–MnO nanoparticles dispersed on amine-grafted silica: Highly efficient nanocatalyst for hydrogen production from additive-free dehydrogenation of formic acid under mild conditions. *Appl. Catal., B* **2015**, *164*, 324–333.
- (33) Silverman, R. B.; Holladay, M. W. *The Organic Chemistry of Drug Design and Drug Action*; Academic Press, 2014.
- (34) Yadav, M.; Akita, T.; Tsumori, N.; Xu, Q. Strong metal-molecular support interaction (SMMSI): Amine-functionalized gold nanoparticles encapsulated in silica nanospheres highly active for catalytic decomposition of formic acid. *J. Mater. Chem.* **2012**, *22*, 12582–12586.
- (35) Mori, K.; Dojo, M.; Yamashita, H. Pd and Pd–Ag Nanoparticles within a Macroreticular Basic Resin: An Efficient Catalyst for Hydrogen Production from Formic Acid Decomposition. *ACS Catal.* **2013**, *3*, 1114–1119.
- (36) Bulut, A.; Yurderi, M.; Karatas, Y.; Say, Z.; Kivrak, H.; Kaya, M.; Gulcan, M.; Ozensoy, E.; Zahmakiran, M. MnOx-Promoted PdAg Alloy Nanoparticles for the Additive-Free Dehydrogenation of Formic Acid at Room Temperature. *ACS Catal.* **2015**, *5*, 6099–6110.
- (37) Sridhar, M.; Van Bokhoven, J. A.; Kröcher, O. Effect of ammonia on the decomposition of ammonium formate over Au/TiO₂ under oxidizing conditions relevant to SCR: Enhancement of formic acid decomposition rate and CO₂ production. *Appl. Catal., A* **2014**, *486*, 219–229.
- (38) McBride, F.; Omer, A.; Clay, C. M.; Cummings, L.; Darling, G. R.; Hodgson, A. Strain relief and disorder in commensurate water layers formed on Pd(111). *J. Phys.: Condens. Matter* **2012**, *24*, 124102.
- (39) Scaranto, J.; Mavrikakis, M. Density functional theory studies of HCOOH decomposition on Pd(111). *Surf. Sci.* **2016**, *650*, 111–120.
- (40) Wang, Y.; Qi, Y.; Zhang, D.; Liu, C. New Insight into the Decomposition Mechanism of Formic Acid on Pd(111): Competing Formation of CO₂ and CO. *J. Phys. Chem. C* **2014**, *118*, 2067–2076.
- (41) Zheng, T.; Stacchiola, D.; Saldin, D. K.; James, J.; Sholl, D. S.; Tysoc, W. T. The structure of formate species on Pd(111) calculated by density functional theory and determined using low energy electron diffraction. *Surf. Sci.* **2005**, *574*, 166–174.
- (42) Kiskinova, M. P.; Bliznakov, G. M. Adsorption and coadsorption of carbon monoxide and hydrogen on Pd(111). *Surf. Sci.* **1982**, *123*, 61–76.
- (43) Erley, W.; Wagner, H. Absolute Co Coverage: Direct Comparison between the (111) and (110) Faces of Ni, Pd, and Pt at 300 K. *J. Chem. Phys.* **1980**, *72*, 2207–2208.
- (44) Ozensoy, E.; Meier, D. C.; Goodman, D. W. Polarization Modulation Infrared Reflection Absorption Spectroscopy at Elevated Pressures: CO Adsorption on Pd(111) at Atmospheric Pressures. *J. Phys. Chem. B* **2002**, *106*, 9367–9371.
- (45) Ozensoy, E.; Min, B. K.; Santra, A. K.; Goodman, D. W. Co Dissociation at Elevated Pressures on Supported Pd Nanoclusters. *J. Phys. Chem. B* **2004**, *108*, 4351–4357.
- (46) Ozensoy, E.; Wayne Goodman, D. Vibrational spectroscopic studies on CO adsorption, NO adsorption CO + NO reaction on Pd model catalysts. *Phys. Chem. Chem. Phys.* **2004**, *6*, 3765–3778.
- (47) Thompson, A. C.; Vaughan, D. *X-ray Data Booklet*; Lawrence Berkeley National Laboratory, University of California Berkeley: CA, 2001; Vol. 8.
- (48) Moulder, J. F. *Handbook of X-ray Photoelectron Spectroscopy*; Physical Electronics, 1995; pp 230–232.
- (49) Mandale, A. B.; Badrinarayanan, S. X-ray photoelectron spectroscopic studies of the semimagnetic semiconductor system Pb_{1-x}Mn_xTe. *J. Electron Spectrosc. Relat. Phenom.* **1990**, *53*, 87–95.
- (50) Hsin-Kuei, H.; Rabalais, J. W. Chemisorption and the Initial Stage of Oxidation on Mn. *Surf. Sci.* **1981**, *107*, 376–390.
- (51) Jenks, C. J.; Chang, S.-L.; Anderegg, J. W.; Thiel, P. A.; Lynch, D. W. Photoelectron spectra of an Al₇₀Pd₂₅Mn₁₅ quasicrystal and the cubic alloy Al₆₀Pd₂₅Mn₁₅. *Phys. Rev. B: Condens. Matter Mater. Phys.* **1996**, *54*, 6301.
- (52) Sandell, A.; Jaworowski, A. J. The Mn 2p core-level photoelectron spectrum of Pd–Mn bimetallic systems on Pd(100). *J. Electron Spectrosc. Relat. Phenom.* **2004**, *135*, 7–14.
- (53) Rader, O.; Mizokawa, T.; Fujimori, A.; Kimura, A. Structure and Electron Correlation of Mn on Ni (110). *Phys. Rev. B: Condens. Matter Mater. Phys.* **2001**, *64*, 165414.
- (54) Rader, O.; Vescovo, E.; Sarma, D. D.; Blügel, S.; Himpfel, F. J.; Kimura, A.; An, K. S.; Mizokawa, T.; Fujimori, A.; Carbone, C. Correlation Satellite Driven by Reduced Dimensionality. *Europhys. Lett.* **1997**, *39*, 429.
- (55) Schieffer, P.; Krembel, C.; Hanf, M.-C.; Gewinner, G. Strong correlation satellites in core level photoemission from Mn in the monolayer range on Ag(001). *J. Electron Spectrosc. Relat. Phenom.* **1999**, *104*, 127–134.
- (56) Li, F.; Parteder, G.; Allegretti, F.; Franchini, C.; Podloucky, R.; Surnev, S.; Netzer, F. P. Two-dimensional manganese oxide nanolayers on Pd(100): the surface phase diagram. *J. Phys.: Condens. Matter* **2009**, *21*, 134008.

- (57) Oku, M.; Hirokawa, K.; Ikeda, S. X-ray photoelectron spectroscopy of manganese–oxygen systems. *J. Electron Spectrosc. Relat. Phenom.* **1975**, *7*, 465–473.
- (58) Di Castro, V.; Polzonetti, G. XPS Study of MnO Oxidation. *J. Electron Spectrosc. Relat. Phenom.* **1989**, *48*, 117–123.
- (59) Foord, J. S.; Jackman, R. B.; Allen, G. C. An X-Ray Photoelectron Spectroscopic Investigation of the Oxidation of Manganese. *Philos. Mag. A* **1984**, *49*, 657–663.
- (60) Strohmeier, B. R.; Hercules, D. M. Surface Spectroscopic Characterization of Manganese/Aluminum Oxide Catalysts. *J. Phys. Chem.* **1984**, *88*, 4922–4929.
- (61) Aoki, A. X-ray Photoelectron Spectroscopic Studies on ZnS: MnF₂ Phosphors. *Jpn. J. Appl. Phys.* **1976**, *15*, 305.
- (62) Biesinger, M. C.; Payne, B. P.; Grosvenor, A. P.; Lau, L. W. M.; Gerson, A. R.; Smart, R. S. C. Resolving Surface Chemical States in XPS Analysis of First Row Transition Metals, Oxides and Hydroxides: Cr, Mn, Fe, Co and Ni. *Appl. Surf. Sci.* **2011**, *257*, 2717–2730.
- (63) Zeng, F.; Pan, Y.; Yang, Y.; Li, Q.; Li, G.; Hou, Z.; Gu, G. Facile Construction of Mn₃O₄-MnO₂ Hetero-Nanorods/Graphene Nanocomposite for Highly Sensitive Electrochemical Detection of Hydrogen Peroxide. *Electrochim. Acta* **2016**, *196*, 587–596.
- (64) Nilekar, A. U.; Greeley, J.; Mavrikakis, M. A Simple Rule of Thumb for Diffusion on Transition-Metal Surfaces. *Angew. Chem., Int. Ed.* **2006**, *45*, 7046–7049.
- (65) Kovács, I.; Kiss, J.; Kónya, Z. The Potassium-Induced Decomposition Pathway of HCOOH on Rh(111). *Catalysts* **2020**, *10*, 675.